J. Fluid Mech. (2021), *vol*. 928, A37, doi:10.1017/jfm.2021.849

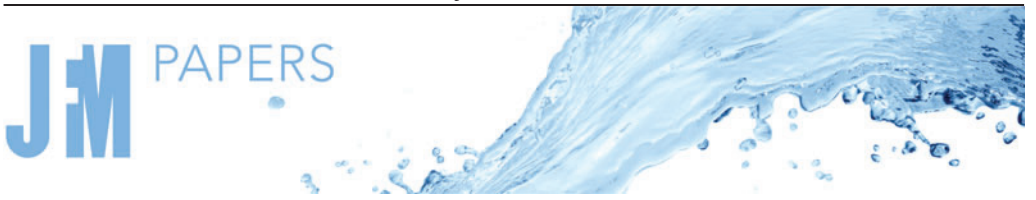

Richtmyer–Meshkov instability on two-dimensional multi-mode interfaces

Yu Liang[1,2], Lili Liu[1], Zhigang Zhai[1,†], Juchun Ding[1], Ting Si[1] and Xisheng Luo[1,†]

[1]Advanced Propulsion Laboratory, Department of Modern Mechanics, University of Science and Technology of China, Hefei 230026, PR China

[2]NYUAD Research Institute, New York University Abu Dhabi, Abu Dhabi 129188, UAE

(Received 14 February 2021; revised 1 August 2021; accepted 23 September 2021)

Shock-tube experiments on eight kinds of two-dimensional multi-mode air–SF_6 interface with controllable initial conditions are performed to examine the dependence of perturbation growth on initial spectra. We deduce and demonstrate experimentally that the amplitude development of each mode is influenced by the mode-competition effect from quasi-linear stages. It is confirmed that the mode-competition effect is closely related to initial spectra, including the wavenumber, the phase and the initial amplitude of constituent modes. By considering both the mode-competition effect and the high-order harmonics effect, a nonlinear model is established based on initial spectra to predict the amplitude growth of each individual mode. The nonlinear model is validated by the present experiments and data in the literature by considering diverse initial spectra, shock intensities and density ratios. Moreover, the nonlinear model is successfully extended based on the superposition principle to predict the growths of the total perturbation width and the bubble/spike width from quasi-linear to nonlinear stages.

Key words: shock waves, turbulent mixing

1. Introduction

Richtmyer–Meshkov (RM) instability is initiated when a shock wave interacts with an interface between two fluids of different densities (Richtmyer 1960; Meshkov 1969), and further induces mushroom-shaped flow structures such as bubbles (light fluids penetrating into heavy ones) and spikes (heavy fluids penetrating into light ones), which finally may cause a flow transition to turbulent mixing (Zhou, Robey & Buckingham 2003; Zhou 2007; Zhou *et al.* 2019). Over the past few decades, the RM instability has become a subject of intensive research due to its crucial role in various industrial and scientific fields such

† Email addresses for correspondence: sanjing@ustc.edu.cn, xluo@ustc.edu.cn

as inertial confinement fusion (ICF) (Lindl *et al.* 2014) and supernova explosion (Kuranz *et al.* 2018). For example, the RM instability determines the seeds of Rayleigh–Taylor (RT) instability (Rayleigh 1883; Taylor 1950) that develops during the implosion in ICF (Goncharov 1999). The mixing of hot fuel inside with cooler shell material outside, induced by RM and RT instabilities in the target of ICF, significantly reduces and even eliminates the thermonuclear yield (Miles *et al.* 2004). The RM instability on a single-mode interface has been extensively studied due to its fundamental significance (Brouillette 2002; Zhou 2017*a*,*b*; Zhai *et al.* 2018). However, the initial perturbation in reality is essentially multi-mode with wavenumbers spanning many orders of magnitude, and whether the perturbation growth of a multi-mode RM instability depends on the initial spectrum or not is crucial to ICF (Miles *et al.* 2004) but remains unclear.

Theoretically, there are mainly six kinds of models describing the perturbation growth of a multi-mode interface: the linear model, the modal model, the potential model, the vortex model, the perturbation expansion model and the group theory approach. Based on the principle that each individual mode develops independently in linear stages, Mikaelian (2005) proposed the linear model to describe the multi-mode interface evolution by summing the time-varying amplitude growth of each mode. Haan (1989) found that the constituent modes with similar wavelengths of a multi-mode interface add up to create an effective local large amplitude, and, therefore, the onset of the nonlinear stage of a multi-mode perturbation is earlier than that of the classical single-mode case. Subsequently, Haan (1991) proposed the modal model with second-order accuracy to quantify the mode-competition effect on the perturbation growth of each mode in the early nonlinear stage. The modal model and its extended types have achieved a wide range of validation in RT instability issues (Remington *et al.* 1995; Ofer *et al.* 1996; Elbaz & Shvarts 2018), but their application to the RM instability is still lacking. Assuming that mode competition is absent before a bubble reaches its asymptotic growth, the potential model was proposed by Alon *et al.* (1994) and Layzer (1955) to predict the eventual average bubble distribution and the growth rate. However, the potential model is invalid when the Atwood number (defined as $A = (\rho_2 - \rho_1)/(\rho_2 + \rho_1)$, with ρ_1 and ρ_2 being the densities of light fluid and heavy fluid, respectively) is low. When the Atwood number approaches zero, the vortex model (Jacobs & Sheeley 1996) was adopted by Rikanati, Alon & Shvarts (1998) to make up the bubble asymptotic growth rate. Note that both the potential model (Alon *et al.* 1994, 1995; Oron *et al.* 2001) and the vortex model (Rikanati *et al.* 1998) involve a self-similar growth of the bubble front which is independent of the initial spectrum, and both models obtain a $1/t$ decay for the late-time bubble growth rate in a multi-mode RM instability. The perturbation expansion model developed by Zhang & Sohn (1997) was extended by Vandenboomgaerde, Gauthier & Mügler (2002) to predict the early nonlinear amplitude growth of the constituent modes of a multi-mode interface by retaining only the terms with the highest power in time. The group theory approach (Abarzhi 2008, 2010; Pandian, Stellingwerf & Abarzhi 2017) identifies the connection between the symmetry properties of the interface morphology and the relative phases of waves constituting the interface perturbation.

Experimentally, shock-tube experiments were performed to investigate two-bubble competition (Sadot *et al.* 1998), and the results showed that the growth of the larger (or smaller) bubble is promoted (or suppressed). Dimonte & Schneider (2000) conducted a series of three-dimensional linear electric motor experiments to investigate multi-mode RT and RM instabilities, and found that the density ratio has a limited effect on the self-similar growth factor for the bubble. When the density ratio is large, the self-similar growth factor for the spike is clearly larger than that for the bubble counterpart.

The multi-mode RM instability of two liquids was investigated by Niederhaus & Jacobs (2003), and the development of the multi-mode perturbation was found to be strongly dependent on the relative amplitudes of initial modes. The growth of the multi-mode interface perturbation created by the gas curtain technique shows a weak dependence on the initial conditions (Balasubramanian, Orlicz & Prestridge 2013). Experiments of a dual-mode interface RM instability under high-Mach-number conditions have been performed (Di Stefano *et al.* 2015*a*,*b*), and the results indicated that new modes are generated from the mode-competition effect, and the perturbations of these modes grow and saturate over time. The dual-mode RM instability under weak shock conditions was also considered, from which the mode-competition effect on the RM instability development cannot be ignored when the wavenumber of one constituent mode is twice that of the other constituent mode (Luo *et al.* 2020). The mixing of a multi-mode interface was investigated by Mohaghar *et al.* (2017) using density and velocity statistics, and the flow shows a distinct memory of initial conditions, the long-wavelength perturbation having a strong influence on the interface development. Recently, developments of quasi-single-mode interfaces created by the soap film technique in the early nonlinear stage have been studied, and the effect of high-order modes on the perturbation growth was highlighted to distinguish from single-mode perturbation (Liang *et al.* 2019). A near-sinusoidal interface dominated by one mode was generated by a novel membraneless technique where cross-flowing air was separated from SF_6 by an oscillating splitter plate (Mansoor *et al.* 2020), and the effects of the initial amplitude on the perturbation width growth and mixing transition have been discussed, and earlier mixing transitions for higher amplitude-to-wavelength ratio cases are noted from experiments.

Numerically, it is commonly realized that the phases of the constituent modes influence multi-mode perturbation growth (Vandenboomgaerde *et al.* 2002; Miles *et al.* 2004; Pandian *et al.* 2017). Besides, the self-similar growth factor of the late-time RM instability has a dependence on the scale of the initial spectrum. Specifically, a broadband perturbation leads to a larger bubble growth factor than a narrowband counterpart (Thornber *et al.* 2010; Liu & Xiao 2016; Thornber 2016; Groom & Thornber 2020).

Although significant progress on the multi-mode RM instability has been made, the quantitative relation between initial conditions and perturbation growth is still unclear mainly because a general nonlinear theory for predicting the multi-mode perturbation width growth is absent, and elaborate experiments on the multi-mode RM instability with controllable initial conditions are very limited. In our previous work, the extended soap-film technique was utilized to create a classical two-dimensional (2-D) single-mode perturbation (Liu *et al.* 2018), a 2-D multi-mode interface dominated by only one mode (Liang *et al.* 2019) and a 2-D multi-mode interface dominated by two modes (Luo *et al.* 2020). The initial perturbations of these interfaces were precisely designed and the initial conditions were well controlled. In this work, a 2-D complex multi-mode interface constituted of various modes is first formed, and shock-tube experiments on the developments of eight kinds of air–SF_6 multi-mode interface are performed. Then, new nonlinear theories based on the initial spectrum, shock intensity and density ratio are proposed to predict each mode amplitude growth and the total perturbation width growth of a 2-D multi-mode interface.

2. Experimental method

The extended soap-film technique, which has been widely used in our previous work (Ding *et al.* 2017; Liu *et al.* 2018; Liang *et al.* 2019), is adopted to generate a periodic

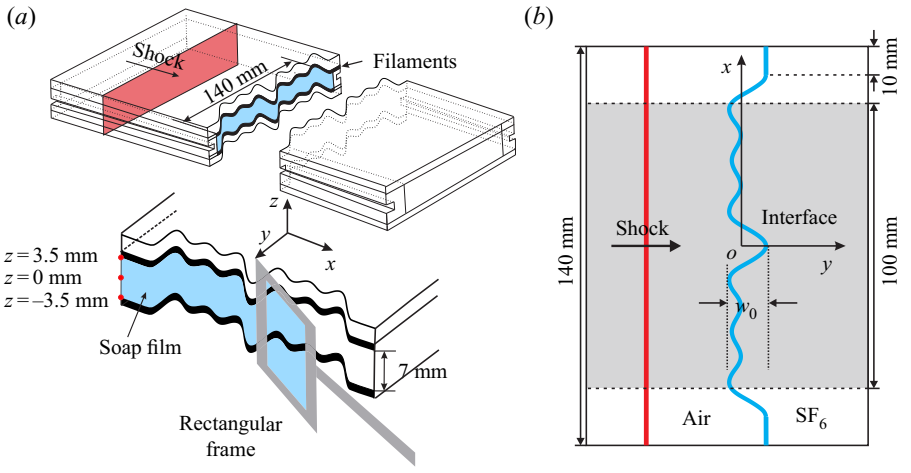

Figure 1. Schematics of soap-film interface generation (*a*) and the initial configuration (*b*).

multi-mode interface with a controllable initial shape to separate SF_6 from air. Such a technique can largely eliminate the short-wavelength perturbations, diffusion layer and three-dimensionality of the formed interface (Liu *et al.* 2018; Liang *et al.* 2019). As shown in figure 1(*a*), two transparent devices with an inner height of 7.0 mm and a width of 140.0 mm are first made using acrylic plates (3.0 mm in thickness). A groove (0.7 mm in thickness and 0.5 mm in width) with a multi-mode shape is then manufactured on the internal side of each plate by a high-precision engraving machine. Then, two thin filaments (1.0 mm in thickness and 0.5 mm in width) with the same multi-mode shape are mounted into the grooves of the upper and lower plates, respectively, to produce desired constraints. Therefore, the bulging of the filament into the flow is less than 0.3 mm, and has a negligible effect on the flow field. A small rectangular frame wetted by soap solution (78 % distilled water, 2 % sodium oleate and 20 % glycerine by mass) is pulled along the filaments, and a quasi-2-D soap-film interface is immediately generated, as shown in figure 1(*a*). Subsequently, the auxiliary framework is gently inserted until it is completely connected to the corresponding device. After that, the framework with a soap film on its surface is slowly inserted into the test section of the shock tube. To form an air–SF_6 interface, the air on the right-hand side of the interface is replaced by SF_6. To minimize the effect of the shock-tube walls on interface evolution, a short flat part with 10 mm on each side of the perturbed interface is adopted, as sketched in figure 1(*b*), and its effect on the interface evolution is limited (Luo *et al.* 2019).

In the Cartesian coordinate system, as sketched in figure 1(*b*), the multi-mode interface investigated can be described as a sum of three cosine modes:

$$y = \sum_{1}^{3} a_{k_n}^0 \cos(k_n x + \phi_{k_n}), \quad x \in [-60, 60]\,\text{mm}, \tag{2.1}$$

where $a_{k_n}^0$, k_n and ϕ_{k_n} respectively denote the initial amplitude, wavenumber and phase of the nth constituent mode with $n = 1$, 2 and 3. To illustrate the influences of the initial amplitude, wavenumber and relative phase on the 2-D multi-mode RM instability, eight different kinds of multi-mode interface are designed in this work. The initial spectrum and the initial perturbation width (w_0, sketched in figure 1*b*) of the multi-mode interface in

Case	$a^0_{k_1}$	$a^0_{k_2}$	$a^0_{k_3}$	k_1	k_2	k_3	ϕ_{k_1}	ϕ_{k_2}	ϕ_{k_3}	$a^0_{k_1}k_1$	$a^0_{k_2}k_2$	$a^0_{k_3}k_3$	w_0	w_{0b}	w_{0s}
IP-s	1.0	1.0	1.0	105	209	314	0	0	0	0.1	0.2	0.3	4.3	3.0	1.3
k_3AP-s	1.0	1.0	1.0	105	209	314	0	0	π	0.1	0.2	0.3	3.5	1.5	2.0
k_2AP-s	1.0	1.0	1.0	105	209	314	0	π	0	0.1	0.2	0.3	4.3	1.3	3.0
AP-s	1.0	1.0	1.0	105	209	314	0	π	π	0.1	0.2	0.3	3.5	2.0	1.5
IP-h	3.0	2.0	1.0	105	209	314	0	0	0	0.3	0.4	0.3	8.0	6.0	2.0
k_3AP-h	3.0	2.0	1.0	105	209	314	0	0	π	0.3	0.4	0.3	7.5	4.0	3.5
k_2AP-h	3.0	2.0	1.0	105	209	314	0	π	0	0.3	0.4	0.3	8.0	2.0	6.0
AP-h	3.0	2.0	1.0	105	209	314	0	π	π	0.3	0.4	0.3	7.5	3.5	4.0

Table 1. Initial spectrum and initial perturbation width of multi-mode interfaces formed in the present work. Here $a^0_{k_n}$, k_n and ϕ_{k_n} denote the initial amplitude, wavenumber and phase of the nth constituent mode, respectively; w_0, w_{0b} and w_{0s} denote the initial total perturbation width, bubble width and spike width of the multi-mode interface, respectively. The unit for the amplitude and width is mm and for the wavenumber is m^{-1}.

different cases are listed in table 1. In this work, ϕ_{k1} is kept as 0 and ϕ_{k2} and ϕ_{k3} are varied. For convenience, the following notation is adopted: $\phi_{k2} = \phi_{k3} = 0$ (in-phase (IP) case); $\phi_{k2} = \phi_{k3} = \pi$ (anti-phase (AP) case); $\phi_{k2} = 0$, $\phi_{k3} = \pi$ (k_3AP case); $\phi_{k2} = \pi$, $\phi_{k3} = 0$ (k_2AP case). The influence of the initial amplitude of mode k_n on the RM instability can be studied by varying $a^0_{k_n}k_n$ (Mansoor *et al.* 2020; Sewell *et al.* 2021). In this work, the cases of IP-s, k_3AP-s, k_2AP-s and AP-s are classified as small-w_0 cases, whereas the cases of IP-h, k_3AP-h, k_2AP-h and AP-h are classified as large-w_0 cases.

The experiments are performed in a horizontal shock tube with a 140 mm × 13 mm cross-sectional area. This type of tube has been widely used in shock–interface interaction studies (Luo, Wang & Si 2013; Zhai *et al.* 2014; Luo *et al.* 2015; Ding *et al.* 2017). The ambient pressure and temperature are 101.3 kPa and 299.5 ± 1.0 K, respectively. In experiments, the incident shock wave with velocity (v_s) of 409 ± 1 m s^{-1} (the incident shock Mach number (M) is 1.18) moves from air to SF_6. The ambient air is considered as pure and the test gas is a mixture of air and SF_6, the mass fraction of SF_6 being 0.97 ± 0.01 calculated according to one-dimensional gas dynamics theory. Meanwhile, the transmitted shock velocity (v_t) and the speed jump of the interface (Δv) can be calculated as 182 ± 1 m s^{-1} and 65.5 ± 0.5 m s^{-1}, respectively. The post-shock Atwood number A^+ (defined as $A^+ = (\rho_2^+ - \rho_1^+)/(\rho_2^+ + \rho_1^+)$, with ρ_2^+ and ρ_1^+ being the densities of shocked test gas and air, respectively) is 0.66 ± 0.01. The flow field is monitored using high-speed schlieren photography. The frame rate of the high-speed video camera (FASTCAM SA5, Photron Limited) is 62 500 f.p.s. with a shutter time of 1 μs. The spatial resolution of the schlieren images is 0.4 mm pixel^{-1}. The visualization window of the flow field is within the range $x \in [-50, 50]$ mm, as shown with the grey zone in figure 1(*b*). For each case, at least three experimental runs are performed, and the experiments have a good repeatability. The relative differences of the data among diverse experimental runs are within 3 %.

The three-dimensional feature of the initial soap-film interface is discussed. Because the gases on both sides of the interface are at ambient pressure, the soap-film interface formed has a zero mean curvature, and the geometry can be characterized as minimum surface (Luo *et al.* 2013; Liang *et al.* 2021). For instance, half of the perturbation width of the soap-film interface in case IP-h or k_3AP-h is 4 mm (see table 1), indicating that the total amplitude of the soap-film interface on the boundary slice (i.e. $z = \pm 3.5$ mm) is 4 mm.

The maximum wavelength of the soap-film interface is 60 mm, and the interface height is 7 mm. Based on our previous work (Luo *et al.* 2013; Liang *et al.* 2021), the amplitude of the soap film on the symmetry slice (i.e. $z = 0$ mm) is 3.75 mm. Therefore, the amplitude ratio of the symmetry slice over the boundary slice is 93.75 %. The absolute difference between the amplitudes on the symmetry slice and the boundary slice is about 0.25 mm, and is smaller than the size of a schlieren image's pixel. As a result, it is believed that the interface height of 7 mm can reduce the three-dimensional effect in this work.

The boundary layer effect on the interface evolution is also considered. After the incident shock with M of 1.18 impacts the interface, the flow behind the transmitted shock can be regarded as laminar and incompressible. As a result, the displacement thickness of the boundary layer (δ^*) can be approximately calculated using the following expression:

$$\delta^* = 1.72\sqrt{\frac{\mu y_{max}}{\rho \Delta v}}, \tag{2.2}$$

where y_{max} ($\approx$100 mm measured from experiment) is the maximum distance that the interface moves when image recording ends. In this study, $\mu = 1.83 \times 10^{-5}$ Pa s ($= 1.60 \times 10^{-5}$ Pa s) is the viscosity coefficient of the ambient (test) gas, $\rho = 1.2$ kg m^{-3} ($= 5.3$ kg m^{-3}) is the density of the ambient (test) gas and $\Delta v \approx 65.5$ m s^{-1}. According to (2.2), the displacement thickness of the boundary layer is calculated to be about 0.26 mm for ambient gas and 0.12 mm for test gas, which is much smaller than the inner height of the acrylic plates (7.0 mm). Therefore, the effect of the boundary layer on the interface evolution is negligible.

After a shock wave impacts the soap film, the soap solution is atomized into tiny droplets (Cohen 1991; Hosseini & Takayama 2005; Ranjan *et al.* 2005). Our previous work (Luo *et al.* 2013; Si *et al.* 2015; Lei *et al.* 2017) revealed that the dimension of the atomized droplets is within 1–10 μm, and a portion of tiny soap droplets follows the evolving interface nicely and can be utilized for light scattering illuminated by a laser. Besides, it is recommended to mix atomized olive oil droplets with a diameter of around 1 μm with SF_6 when injecting the test gas into the test section of a shock tube. Using the atomized soap droplets and oil droplets as tracer particles, it is worth looking forward to adopting a particle image velocimetry system to capture the velocity and vorticity contours of an evolving interface initially generated with soap-film technology.

3. Results and discussion

3.1. *Experimental observation and quantitative results*

The schlieren images of the shocked multi-mode interface for small-w_0 cases are shown in figure 2. It is evident that the phases of the constituent modes greatly affect the initial interface shape and the later interface evolution. Taking the IP-s case as an example, after the transmitted shock just leaves the interface, the shocked interface retains its initial shape (69 μs). Then, the perturbation on the interface grows gradually but the interface remains single-valued, which indicates that the interface evolves in early nonlinear stages. Subsequently, vortices appear on the spikes, and the interface morphology acts as multi-valued (261 μs). Due to the bubble-merging process (Sadot *et al.* 1998), the large spike between the large bubble and small bubble skews towards the large bubble, whereas the small spike between two large spikes remains symmetric (581 μs), which qualitatively agrees with the group theory analysis (Abarzhi 2008, 2010; Pandian *et al.* 2017). Finally, the scales of vortices are comparable to the total perturbation width, and the interfacial morphology shows a strong nonlinearity (1061 μs).

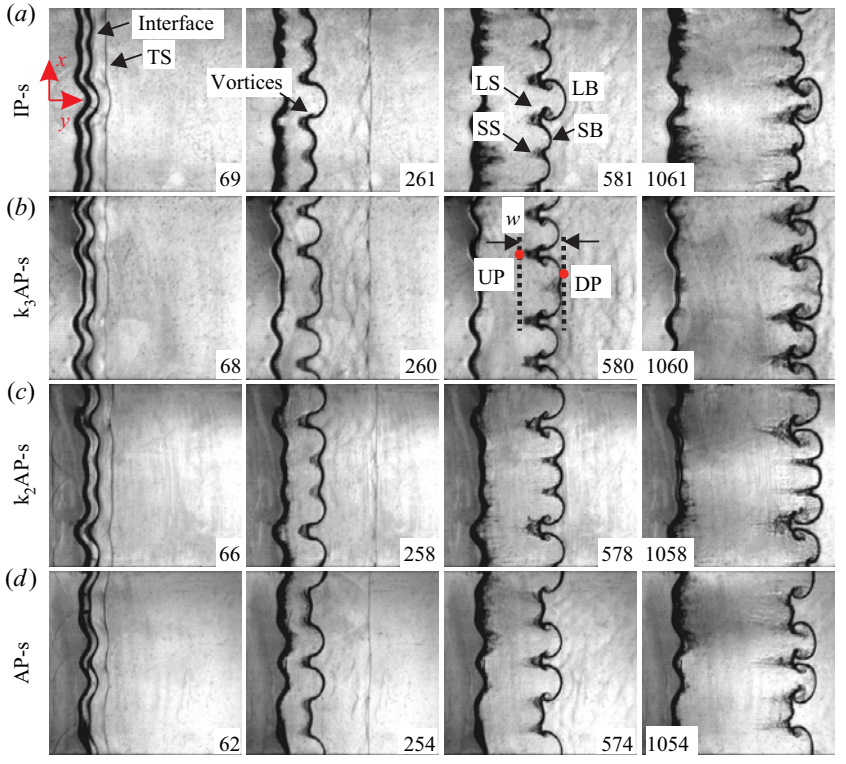

Figure 2. Schlieren images of multi-mode interface evolution for small w_0 cases. TS, transmitted shock; w, interface perturbation width; LS, large spike; LB, large bubble; SS, small spike; SB, small bubble; UP, upstream point of interface; DP, downstream point of interface. Numbers denote time in μs, and similarly hereinafter.

The Schlieren images of the shocked multi-mode interface for large-w_0 cases are shown in figure 3. The interface morphologies in large-w_0 cases are qualitatively similar to the corresponding small-w_0 ones. However, for the large-w_0 cases, there is a greater misalignment between the pressure gradient of the shock wave and the density gradient of the interface, resulting in more baroclinic vorticity production and the earlier appearance of vortices. Besides, at late time in the k_2AP case (1062 μs), the spike structures on the multi-valued interface break, and the whole interface becomes chaotic, which indicates that the transition may occur earlier when the initial interface amplitude is larger (Mohaghar *et al.* 2019; Mansoor *et al.* 2020).

The captured interface morphology is distinct such that the interface contours in all cases can be extracted by an image processing program, as indicated by the insets in figures 4 and 5. The mean y coordinate in each image is taken as the average position of the local interface. Spectrum analysis is then performed on the averaged interface contour before the interface becomes multi-valued, and the amplitudes of three constituent modes are acquired, as shown in figures 4 and 5. Time is normalized as $\tau_n = k_1|v_{k_n}^R|t$, where $v_{k_n}^R$ is the Richtmyer growth rate of mode k_n calculated by the impulsive theory (Richtmyer 1960):

$$v_{k_n}^R = Z_c k A^+ \Delta v a_{k_n}^0 \cos(\phi_{k_n}), \tag{3.1}$$

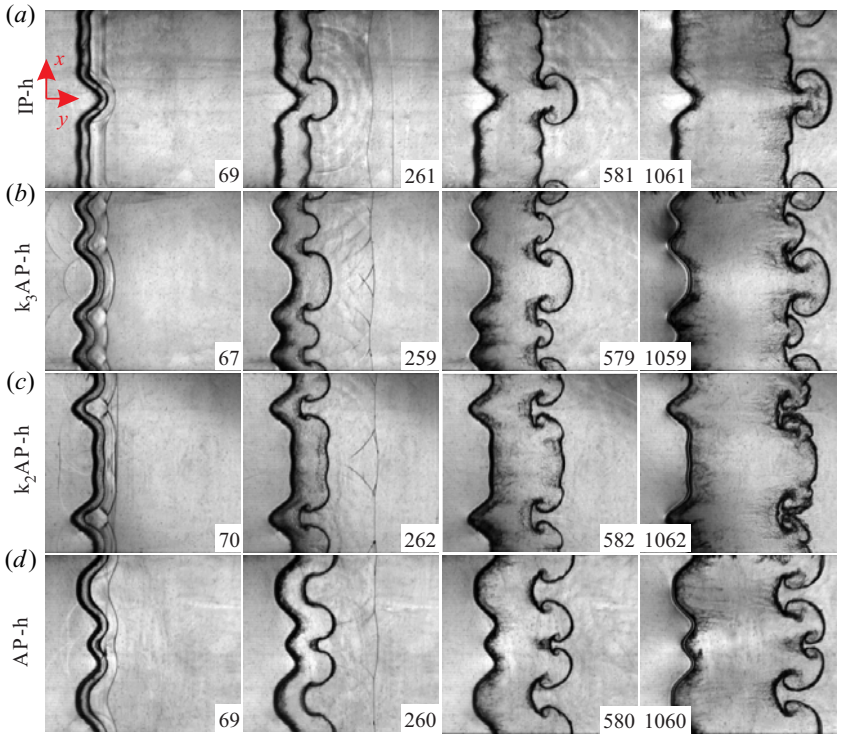

Figure 3. Schlieren images of the multi-mode interface evolution for large-w_0 cases.

in which Z_c $(= 1 - \Delta v/v_s)$ is the shock compression factor and is equal to 0.84 in all cases. In the present coordinate system, $v_{k_n}^R$ is positive if $\phi_{k_n} = 0$, but becomes negative if $\phi_{k_n} = \pi$. The amplitude is scaled as $\eta_n = k_1|a_{k_n}(t) - Z_c a_{k_n}^0 \cos(\phi_{k_n})|$, with $a_{k_n}(t)$ the time-varying amplitude of mode k_n.

In small-w_0 cases, as shown in figure 4, it is clear that the dimensionless amplitudes of modes k_1 and k_2 are larger than those of mode k_3 in IP-s and AP-s cases, but smaller than those of mode k_3 in k_3AP and k_2AP cases. In other words, the low-order modes (modes k_1 and k_2) in IP-s and AP-s cases dominate the flow, whereas the high-order mode (mode k_3) in k_3AP and k_2AP cases dominates the flow, which agree with the observations in figure 2. For example, in the IP-s case in figure 2(a), the late-time interface is dominated by long-wavelength structures (a large bubble and two groups of large and small spikes), but in the k_3AP case in figure 2(b), the late-time interface is dominated by four short-wavelength structures (four pairs of spikes and bubbles). Therefore, the mode-competition effect plays a role in the amplitude development of the constituent modes in early stages. Since the small perturbation hypothesis is satisfied for each constituent mode, the impulsive theory should be valid to predict the amplitude growth of each constituent mode if the mode-competition effect is ignored. However, compared with the predictions of the impulsive theory, in the IP-s case, mode k_1 development is promoted but mode k_3 development is suppressed, while mode k_2 development is not obviously influenced by the mode-competition effect. Differently, in the k_3AP-s case, the developments of both modes k_1 and k_2 are suppressed, while the development of mode k_3 is not obviously influenced by the mode-competition effect. Therefore, the

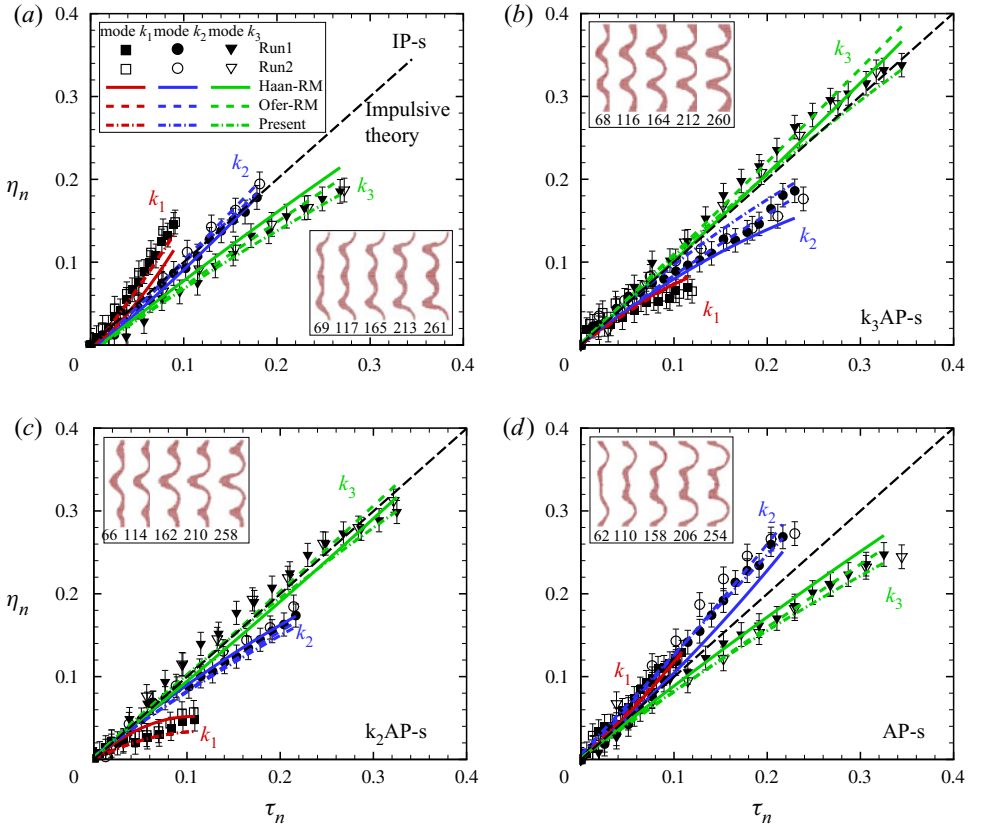

Figure 4. The dimensionless amplitudes of three constituent modes obtained from small-w_0 cases. The insets show the interface contours for the spectrum analysis in which numbers indicate time in μs. Run1 and run2 represent typical experimental runs. The black dashed line represents the impulsive theory (Richtmyer 1960). The coloured solid lines, dashed lines and dash-dotted lines represent the amplitudes of three constituent modes calculated by the Haan-RM model (3.4), the Ofer-RM model (3.7) and the present model (3.10), respectively, and similarly hereinafter.

mode-competition effect is greatly influenced by the initial wavenumber and the initial phase of the constituent mode.

In large-w_0 cases, as shown in figure 5, similar to the corresponding small-w_0 cases, the amplitudes of both modes k_1 and k_2 are larger than those of mode k_3 in IP-h and AP-h cases, but smaller than those of mode k_3 in k_3AP-h and k_2AP-h cases. However, compared with the impulsive theory, mode k_2 development in the IP-h case is suppressed whereas mode k_3 development in the k_3AP-h case is promoted by the mode-competition effect, which is different from the results of corresponding small-w_0 cases. Therefore, the initial amplitude of the constituent mode also affects the mode-competition effect. In summary, the effect of mode competition is closely related to the initial spectra, including the wavenumber, the phase and the initial amplitude of the constituent modes.

Generally, the linear stage is defined by the fact that Fourier modes evolve separately (Drazin & Reid 2004; Chandrasekhar 2013). Because it is difficult to obtain the starting point of the linear stage in reality, usually used within the framework of RM instability is that the linear stage occurs as long as mode k satisfies $a_k(t)k < \alpha$. This constant α

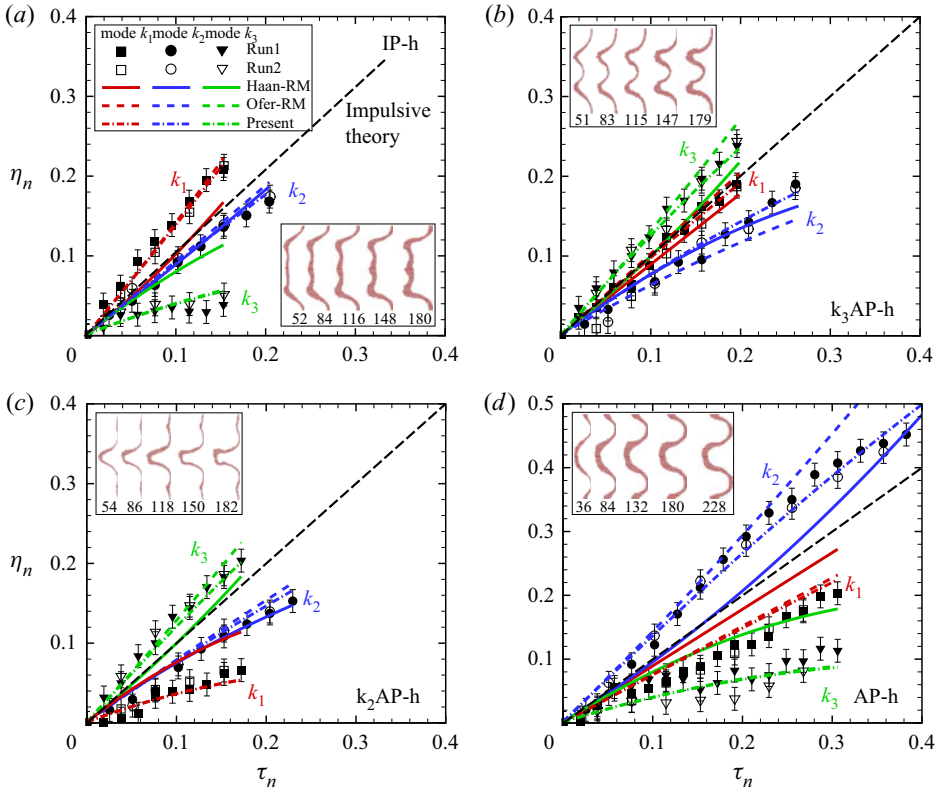

Figure 5. The dimensionless amplitudes of three modes obtained from large-w_0 cases.

depends essentially on the accuracy required. As a result, it is generally accepted that the necessary condition of the linear RM instability is $a_k^0 k \ll 1$ (Mügler & Gauthier 1998; Collins & Jacobs 2002; Mikaelian 2003; Niederhaus & Jacobs 2003; Mariani *et al.* 2008; Vandenboomgaerde *et al.* 2014; Mansoor *et al.* 2020). However, the linear stage still exists for a very large initial $a_k^0 k$ at the expense of a large reduction in the duration of the linear stage (Rikanati *et al.* 2003; Dell, Stellingwerf & Abarzhi 2015; Zhai *et al.* 2016; Dell *et al.* 2017). It should be noted that there are harmonics growing with time in these large initial α cases but they are (almost) negligible. Therefore, this linear stage within large initial α is actually a quasi-linear stage. As listed in table 2, the criterion of dimensionless time, i.e. τ_n^* $(= k_n |v_{k_n}^R| t)$, of mode k_n between the quasi-linear stage and the nonlinear stage is evaluated from experiments. It is found that τ_n^* of the three initial modes are less than the generally accepted criterion of dimensionless time of 0.7 for the single-mode RM instability (Niederhaus & Jacobs 2003), indicating that the large initial $a_{k_n}^0 k_n$ results in a very short quasi-linear stage and the mode competition advances the nonlinearity of the multi-mode RM instability.

3.2. *Linear and nonlinear theories*

To quantitatively describe the 2-D multi-mode RM instability development, linear and nonlinear theories based on the impulsive theory, the modal model and the interpolation model have been established.

Case	IP-s	k_3AP-s	k_2AP-s	AP-s	IP-h	k_3AP-h	k_2AP-h	AP-h
τ_1^*	0.06	0.07	0.06	0.08	0.13	0.18	0.17	0.22
τ_2^*	0.64	0.32	0.32	0.34	0.36	0.40	0.36	0.52
τ_3^*	0.66	0.72	0.54	0.72	0.30	0.48	0.42	0.66

Table 2. The criterion of dimensionless time (τ_n^*) of mode k_n between the quasi-linear stage and the nonlinear stage.

I. Impulsive theory. If each mode of a multi-mode interface satisfies $|a_k(t)k| \ll 1$, the whole interface evolves linearly. Previous studies (Sadot *et al.* 1998; Mikaelian 2005; Di Stefano *et al.* 2015*a*,*b*; Liang *et al.* 2019) considered that the mode-competition effect is negligible in quasi-linear stages. Therefore, for an initial light–heavy interface, the linear amplitude growth rate (v_k^l) of mode k can be described by the impulsive theory (3.1), i.e. $v_k^l = v_k^R$. For an initial heavy–light perturbed interface, the Richtmyer growth rate should be modified as $v_k^R = (Z_c + 1)kA^+\Delta v a_k^0 \cos(\phi_k)/2$ (Meyer & Blewett 1972).

When a_k^0 is comparable to its wavelength or/and the shock intensity is large, the high-amplitude effect or/and the high-Mach-number effect will inhibit v_k^R (Rikanati *et al.* 2003; Dell *et al.* 2015, 2017; Guo *et al.* 2020). Here, the high-amplitude effect and the high-Mach-number effect are considered independently. Then the modified Richtmyer growth rate (v_k^{MR}) is

$$v_k^{MR} = \beta\Delta v \tanh(R_k v_k^R/\beta\Delta v), \tag{3.2}$$

where R_k $(= 1/[1 + (ka_k^0/3)^{(4/3)}])$ is the reduction factor proposed by Dimonte & Ramaprabhu (2010) to quantify the high-amplitude effect on mode k. For small-w_0 cases, $R_{k_1} = 0.97$, $R_{k_2} = 0.93$ and $R_{k_3} = 0.91$; for large-w_0 cases, $R_{k_1} = 0.91$, $R_{k_2} = 0.88$ and $R_{k_3} = 0.91$. Parameter β $(= 1 - \Delta v/v_t)$ is the reduction factor proposed by Hurricane *et al.* (2000) to quantify the high-Mach-number effect on all modes, and $\beta = 0.64$ in all cases.

II. Modal model. When the mode competition starts to play a role, the interface evolution enters the early nonlinear stage. Haan (1991) first proposed a modal model applicable to the 2-D RT instability, and then deduced the modal model for the 2-D RM instability with zero acceleration ($g = 0$) and assuming $|a_k(t)| \gg |a_k^0|$, i.e. ignoring the initial amplitude terms, as

$$a_k(t) = a_k^l(t) + \frac{1}{2}Ak\sum_{k'} a_{k'}^l(t)a_{k''}^l(t) \times \left(\frac{1}{2} - \hat{\boldsymbol{k}}\cdot\widehat{\boldsymbol{k'}} - \frac{1}{2}\widehat{\boldsymbol{k'}}\cdot\widehat{\boldsymbol{k''}}\right), \tag{3.3}$$

where $\boldsymbol{k''} = \boldsymbol{k} - \boldsymbol{k'}$; $\boldsymbol{k}$, $\boldsymbol{k'}$ and $\boldsymbol{k''} \in \mathbb{R}^2$; and $\hat{\boldsymbol{k}}$ is the unit vector $\boldsymbol{k}/k$. Amplitude $a_k^l(t)$ is the linear amplitude of mode k. Taking the first derivative of (3.3) and using the post-shock physical parameters, the 'Haan-RM' model can be obtained to calculate the early nonlinear amplitude growth rate $v_k^{en}(t)$ of mode k as

$$v_k^{en}(t) = v_k^{MR} + A^+k\left(2\sum_{k'} v_{k'}^{MR}v_{k+k'}^{MR} - \sum_{k'<k} v_{k'}^{MR}v_{k-k'}^{MR}\right)t, \tag{3.4}$$

where k, k' and $k'' \in \mathbb{R}^+$. The first term on the right-hand of the Haan-RM model indicates that the development of each mode of a multi-mode RM unstable interface is still strongly

influenced by its independent perturbation growth. At $t \approx 0$, the Haan-RM model reduces to $v_k^{en}(t) \approx v_k^l = v_k^{MR}$, which indicates that the mode-competition effect is very weak and can be ignored. The second term on the right-hand side is the mode-competition term, and it is evident that as t increases, the mode-competition effect plays a more important role in influencing the RM instability. The first sum term in the mode-competition term represents the generation of mode k from high-order modes and indicates the bubble-merging process. The second sum term in the mode-competition term represents the generation of mode k from the interaction of low-order modes, which is related to the bubble-spike asymmetry and the total mixing rate decrement.

However, the initial amplitude terms cannot be ignored in deducing the modal model for the whole process of the RM instability, especially when the initial amplitude of mode k is large. Now, the modal model for the RM instability including the initial amplitude terms is re-derived. Based on the modal model solved by Ofer *et al.* (1996) to second-order accuracy with $g =$ constant for the RT instability,

$$a_k(t) = a_k^l(t) + \frac{1}{2}Ak\left[\sum_{k'} a_{k'}^l(t)a_{k+k'}^l(t) - \frac{1}{2}\sum_{k'<k} a_{k'}^l(t)a_{k-k'}^l(t)\right], \tag{3.5}$$

we take the second derivative of (3.5) with time, and get

$$\begin{aligned}\frac{\mathrm{d}^2 a_k(t)}{\mathrm{d}t^2} = {} & Agka_k^0 + \frac{1}{2}A^2gk\left\{\sum_{k'}[k'a_{k'}^0 a_{k+k'}^l(t) + 2\sqrt{k'(k+k')}a_{k'}^0 a_{k+k'}^0\right. \\ & + (k+k')a_{k+k'}^0 a_{k'}^l(t)] - \frac{1}{2}\sum_{k'<k}[k'a_{k'}^0 a_{k-k'}^l(t) \\ & \left. + 2\sqrt{k'(k-k')}a_{k'}^0 a_{k+k'}^0 + (k-k')a_{k-k'}^0 a_{k'}^l(t)]\right\}. \end{aligned} \tag{3.6}$$

Similar to Richtmyer (1960), the constant g is replaced by an impulsive acceleration $\delta t\Delta v$ ($\delta t = 0$ when $t = 0$ and $\delta t = 1$ when $t > 0$) and the post-shock physical parameters are adopted. Through integrating (3.6) with time, v_k^{en} for the RM instability can be expressed as a superposition of the linear amplitude growth rate v_k^l and the weakly nonlinear modification $v_k^{wn}(t)$:

$$v_k^{en}(t) = v_k^l + v_k^{wn}(t), \tag{3.7}$$

with

$$\begin{aligned} v_k^l = v_k^{MR} + \frac{1}{2}A^+k & \left\{\sum_{k'}\left[v_{k'}^{MR}Z_c a_{k+k'}^0 + v_{k+k'}^{MR}Z_c a_{k'}^0\left(1 + 2\sqrt{\frac{k}{k'}+1}\right)\right]\right. \\ & \left. -\frac{1}{2}\sum_{k'<k}\left[v_{k'}^{MR}Z_c a_{k-k'}^0 + v_{k-k'}^{MR}Z_c a_{k'}^0\left(1 + 2\sqrt{\frac{k}{k'}-1}\right)\right]\right\} \end{aligned} \tag{3.8}$$

and

$$v_k^{wn}(t) = A^+k\left(\sum_{k'} v_{k'}^{MR}v_{k+k'}^{MR} - \frac{1}{2}\sum_{k'<k} v_{k'}^{MR}v_{k-k'}^{MR}\right)t. \tag{3.9}$$

Here, (3.7)–(3.9) are called the 'Ofer-RM' model. Different from $v_k^l = v_k^{MR}$ indicated by the Haan-RM model, v_k^l in the Ofer-RM model is a superposition of v_k^{MR} with the

Case	$v_{k_1}^{MR}$	$v_{k_1}^{l}$	$v_{k_2}^{MR}$	$v_{k_2}^{l}$	$v_{k_3}^{MR}$	$v_{k_3}^{l}$	$v_{k_4}^{MR}$	$v_{k_4}^{l}$	$v_{k_5}^{MR}$	$v_{k_5}^{l}$	$v_{k_6}^{MR}$	$v_{k_6}^{l}$
IP-s	3.7	5.2	7.1	7.9	10.1	8.8	0	−3.1	0	−2.4	0	−3.4
k_3AP-s	3.7	3.3	7.2	5.1	−10.3	−11.3	0	−0.1	0	2.6	0	−3.7
k_2AP-s	3.7	2.1	−7.2	−6.1	10.3	11.4	0	−3.3	0	2.6	0	−3.7
AP-s	3.7	4.1	−7.1	−9.2	−10.2	−9.5	0	−0.1	0	−2.6	0	−3.6
IP-h	10.1	15.8	12.9	14.2	10.1	5.2	0	−10.7	0	−4.9	0	−3.6
k_3AP-h	10.4	12.2	13.2	5.2	−10.4	−15.9	0	−1.8	0	5.1	0	−3.8
k_2AP-h	10.1	4.9	−12.9	−12.5	10.1	15.5	0	−10.7	0	4.9	0	−3.6
AP-h	10.3	8.8	−13.4	−21.5	−10.3	−5.2	0	−1.7	0	−4.9	0	−3.6

Table 3. Comparison of the modified Richtmyer growth rate ($v_{k_n}^{MR}$) calculated by (3.2) with the linear amplitude growth rate ($v_{k_n}^{l}$) calculated by (3.7). The unit for the growth rate is m s^{-1}.

mode-competition term that is related to the initial amplitudes of constituent modes. In other words, the mode-competition effect influences each mode perturbation growth in the quasi-linear stage of the multi-mode RM instability, which is different from the previous view that the mode-competition effect can be ignored in the quasi-linear stage (Sadot *et al.* 1998; Mikaelian 2005; Di Stefano *et al.* 2015*a*,*b*; Liang *et al.* 2019). Besides, when $v_k^{en}(t) = 0$, mode k is fully saturated. Here, additional rules introduced by Ofer *et al.* (1996) for the enforced post-saturation treatment in calculating $v_k^{en}(t)$ are adopted: (i) no weakly nonlinear modifications of a saturated mode to low-order modes and (ii) the phases of the harmonics generated by the saturated modes are opposite.

The predictions from the Haan-RM model and the Ofer-RM model are calculated as shown in figures 4 and 5. For small-w_0 cases, because the initial amplitudes of three modes are small, both models give reasonable predictions of the experimental results. Differently, for large-w_0 cases, the Ofer-RM model provides a better prediction of the amplitude growth than the Haan-RM model for some constituent modes, such as modes k_1 and k_3 in the IP-h case, mode k_1 in the k_2AP-h case and modes k_1 and k_2 in the AP-h case. Note that the amplitude developments of mode k_1 in the IP-h case and mode k_3 in the AP-h case deviate from predictions of the impulsive theory from the very beginning, which verifies that the mode-competition effect plays an important role in the early evolution of a multi-mode interface. In summary, the Ofer-RM model is more applicable to describing the multi-mode RM instability behaviour in the early nonlinear stage, especially when the initial amplitudes of constituent modes are large. Meanwhile, the present experimental results prove that the linear growth of each mode amplitude is also influenced by the mode-competition effect.

Based on (3.8), v_k^l considering the mode-competition effect is calculated and compared with v_k^{MR} without the mode-competition effect, as listed in table 3 for all cases. The difference between v_k^l and v_k^{MR} is larger in large-w_0 cases than in small-w_0 cases. According to the modal analysis (Haan 1991; Ofer *et al.* 1996; Miles *et al.* 2004), the coupling of constituent modes will generate new harmonics. In our experiments, k_2 and k_3 are integral multiples of k_1, and thus no modes with wavenumber lower than k_1 will be generated (Miles *et al.* 2004). However, three new harmonics with higher order, i.e. harmonics k_4 ($= k_1 + k_3$), k_5 ($= k_2 + k_3$) and k_6 ($= k_3 + k_3$), are generated if only the first generation of new harmonics is considered (Ofer *et al.* 1996). The values of v_k^l for the three generated harmonics are listed in table 3. It is evident that the new generated harmonics cannot be ignored in the multi-mode RM instability development in early stages.

III. Interpolation model. Although the Ofer-RM model generally gives a better prediction than the Haan-RM model in large-w_0 cases, it still underestimates mode k_2 development in the k_3AP-s case and overestimates mode k_2 development in the AP-h case when t is large. According to the Ofer-RM model, when $t \to \infty$, v_k^l is neglected and v_k^{en} is proportional to t as long as v_k^{wn} is non-zero. Actually, in the consideration of classical single-mode RM instability, the late nonlinear amplitude growth rate (v_k^{ln}) of mode k should be t^{-1} decay (Hecht, Alon & Shvarts 1994; Alon *et al.* 1995; Mikaelian 1998) because of the suppression of high-order (three orders or greater) harmonics generated by mode k itself (Velikovich & Dimonte 1996; Zhang & Sohn 1997; Nishihara *et al.* 2010; Velikovich, Herrmann & Abarzhi 2014). In the multi-mode RM instability counterparts, the perturbation width growth in the fully turbulent stage is proportional to t^θ as a result of bubble merging (Alon *et al.* 1994, 1995). Although the value of θ has not been unified, it should be much lower than 1.0, as reviewed by Zhou (2017*a*,*b*). Therefore, the perturbation width growth rate of a multi-mode interface should be proportional to $t^{\theta-1}$ with $-1 < (\theta - 1) < 0$ in the fully turbulent stage. As a result, the Ofer-RM model with second-order accuracy is not applicable to describing the late-time 2-D multi-mode RM instability, and its scope should be extended by considering the suppression from high-order harmonics.

An interpolation model proposed by Dimonte & Ramaprabhu (2010) (DR model) for predicting 2-D single-mode amplitude growth covers the entire time domain from the early to late nonlinear stages of the RM instability, and it has been well verified by several independent experiments (Dimonte *et al.* 1996; Sadot *et al.* 1998; Niederhaus & Jacobs 2003; Jacobs & Krivets 2005) through considering diverse amplitude-to-wavelength ratios, shock intensities and density ratios. In this work, the scope of the Ofer-RM model is extended in combination with the DR model, and then v_k^{ln} can be expressed as an average of the bubble amplitude growth rate $v_{kb}^{ln}(t)$ with the spike amplitude growth rate $v_{ks}^{ln}(t)$ of mode k:

$$v_k^{ln}(t) = \tfrac{1}{2}[v_{kb}^{ln}(t) + v_{ks}^{ln}(t)], \tag{3.10}$$

with

$$\left.\begin{aligned} v_{kb/ks}^{ln}(t) &= v_k^{en}(t)\frac{1 + (1 \mp |A^+|)|kv_k^{en}(t)t|}{1 + C_{b/s}|kv_k^{en}(t)t| + (1 \mp |A^+|)F_{b/s}|kv_k^{en}(t)t|^2}, \\ C_{b/s} &= \frac{4.5 \pm |A^+| + (2 \mp |A^+|)(ka_0^k)}{4}, \quad F_{b/s} = 1 \pm |A^+|. \end{aligned}\right\} \tag{3.11}$$

Finally, (3.2), (3.7) and (3.10) constitute the 'present' model for describing the 2-D multi-mode RM instability in this work. Notably, the self-similar law shows that the perturbation width growth rate of a multi-mode interface in the fully turbulent stage has a $t^{\theta-1}$ dependence and therefore approaches zero when $t \to \infty$. According to (3.10) and (3.11), when $t \to \infty$, $v_k^{ln}(t)$ also approaches zero but shows a t^{-1} dependence, i.e. $\theta = 0$, which violates the self-similar law. However, the t^{-1} asymptotic dependence agrees with the potential model (Alon *et al.* 1994, 1995; Oron *et al.* 2001), the vortex model (Rikanati *et al.* 1998) and recent experimental findings (Mansoor *et al.* 2020).

The predictions of the present model for our experiments are shown in figures 4 and 5, and a good agreement between them is achieved. Besides, data from literature are extracted to validate the present model. First, the numerical results from figures 9 and 10 of Vandenboomgaerde *et al.* (2002) with both M (= 1.0962) and A^+ (= 0.764)

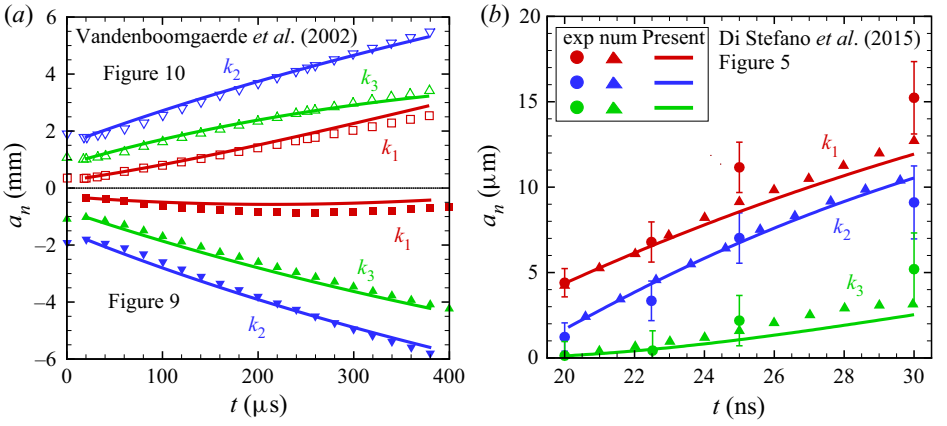

Figure 6. The amplitudes of modes obtained from (*a*) the numerical results in Vandenboomgaerde *et al.* (2002) and (*b*) the experimental and numerical results in Di Stefano *et al.* (2015*b*). Coloured lines represent the predictions calculated with the present model.

similar to those in our experiments are extracted, as shown in figure 6(*a*). The initial interface consists of three modes: $a^0_{k_1} = 0.35 \times 10^{-3}$, $a^0_{k_2} = 1.9055 \times 10^{-3}$ and $a^0_{k_3} = 1.072 \times 10^{-3}$ m; $k_1 = 274.855\,\mathrm{m}^{-1}$, $k_2 = 3k_1/7$ and $k_3 = 4k_1/7$. For the data in figure 9 of Vandenboomgaerde *et al.* (2002), $\phi_1 = \phi_2 = \phi_3 = 0$, while for the data in figure 10, $\phi_1 = \phi_2 = \phi_3 = \pi$. For these two cases, $R_{k_1} = 0.97$, $R_{k_2} = 0.93$ and $R_{k_3} = 0.95$; $\beta = 0.80$. It is found that the predictions of the present model agree well with all the numerical results (Vandenboomgaerde *et al.* 2002). Further, the experimental and numerical results (Di Stefano *et al.* 2015*b*) with a much larger M (= 8) and a smaller A^+ (= 1/3) compared with our experimental conditions are predicted by the present model. The initial interface in the literature (Di Stefano *et al.* 2015*b*) consists of two modes: $a^0_{k_1} = 5 \times 10^{-6}$ m, $a^0_{k_2} = 0.5a^0_{k_1}$; $k_1 = 6.28 \times 10^4\,\mathrm{m}^{-1}$, $k_2 = 2k_1$; $\phi_1 = 0$, $\phi_2 = \pi$; $R_{k_1} = 0.91$, $R_{k_2} = 0.91$; $\beta = 0.35$. The amplitude growths of the two constituent modes and the harmonic k_3 generated by the coupling of modes k_1 and k_2 are extracted from figure 5 of Di Stefano *et al.* (2015*b*), as shown in figure 6(*b*). It is found that not only the constituent mode amplitudes, but also the generated new harmonic amplitude are well predicted by the present model. Overall, the present model established in this work by considering both the mode-competition effect and the high-order harmonics effect is applicable to the nonlinear RM instability before the transition.

3.3. *The perturbation width growth*

The memory of the perturbation width growth of a multi-mode interface on its initial spectrum is crucial to RM instability research. The perturbation width $w(t)$ of a multi-mode interface is defined as the streamwise distance from the upstream point (UP) to the downstream point (DP) of an interface, as shown in figure 2(*b*). The variations of the perturbation width measured from the schlieren images for small- and large-w_0 cases are shown in figures 7(*a*) and 8(*a*), respectively. The time is normalized as $\tau_w = 0.5k_1 v_w^{MR} t$, where $v_w^{MR} = \sum_1^3 v_{k_n}^{MR}[\cos(k_n x_{DP}) - \cos(k_n x_{UP})]$, with x_{UP} and x_{DP} being the x coordinates of UP and DP, respectively. The half of the perturbation width is scaled as $\eta_w = 0.5k_1[w(t) - Z_c w^0]$. To compare the perturbation width between the

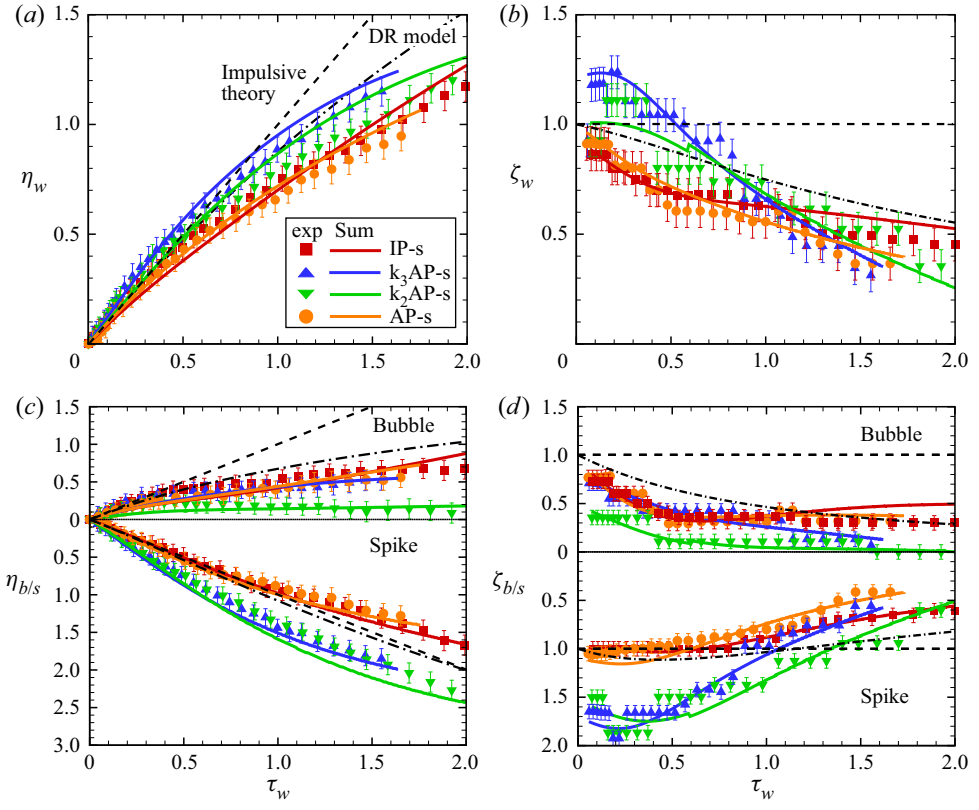

Figure 7. Comparison of the perturbation width (*a*), growth rate of the perturbation width (*b*), widths of bubble and spike (*c*) and width growth rates of bubble and spike (*d*) in small-w_0 cases. Black dashed lines and dash-dotted lines represent the single-mode linear and nonlinear amplitude growth rates calculated by the impulsive theory (Richtmyer 1960) and DR model (Dimonte & Ramaprabhu 2010), respectively. Coloured solid lines represent the predictions from the sum model calculated with (3.12), and similarly hereinafter.

multi-mode interface and the classical single-mode interface, the predictions from the impulsive theory and the DR model are calculated, as shown in figures 7(*a*) and 8(*a*), respectively. It is evident that the perturbation width growth of a multi-mode interface in the early stage ($\tau_w \leq 0.5$) is close to or even larger than the single-mode linear growth, which indicates that the mode-competition effect may enhance the initial growth of the multi-mode perturbation. Later, the perturbation width growth in all cases is smaller than the single-mode linear growth when $\tau_w > 0.7$ and smaller than the single-mode nonlinear growth when $\tau_w > 1.2$. Therefore, the mode-competition effect suppresses the multi-mode interface development at late stages because it enhances local mixing and reduces the global mixing. Besides, the $w(t)$ growth curves in all cases deviate from each other, which indicates that the initial spectrum influences the 2-D multi-mode RM instability until the late nonlinear stage.

To more clearly distinguish the differences of the perturbation growth with diverse initial conditions, through the direct differentiation of the experimental data, the perturbation width growth rate $\dot{w}(t)$ of a multi-mode interface is acquired, and compared with the single-mode linear and nonlinear amplitude growth rates, as shown in figures 7(*b*) and 8(*b*) for all cases. The perturbation width growth rate is scaled as $\zeta_w = \dot{w}_s(t)/v_w^{MR}$. Therefore, the dimensionless single-mode linear growth rate is $\zeta_w = 1$. In small-w_0 cases, $\dot{w}(t)$

in IP-s and AP-s cases is smaller than that of the single-mode growth rate during the whole process. The value of $\dot{w}(t)$ in k_3AP-s and k_2AP-s cases is larger than that of the single-mode counterpart in early times ($\tau_w \leq 0.5$), but smaller than that of the single-mode counterpart in late stages. In large-w_0 cases, differently, $\dot{w}(t)$ in IP-h and k_2AP-h cases is smaller than that of the single-mode growth rate during the whole process. The value of $\dot{w}(t)$ in k_3AP-h and AP-h cases is larger than that of the single-mode counterpart in early times ($\tau_w \leq 0.5$), but smaller than that of the single-mode counterpart in late stages. Therefore, both the phase and amplitude of the constituent modes influence the mode-competition effect on the perturbation width growth of a multi-mode interface. Besides, the growth rate of a multi-mode interface with all modes in-phase is smaller than the counterpart in the classical single-mode case and other multi-mode cases. In addition, under specific conditions, such as in k_3AP-s and k_3AP-h cases, the mode-competition effect promotes the perturbation width growth in early stages.

Compared with the reference moving with the post-shock flow velocity, the width growths of the bubble ($w_b(t)$) and the spike ($w_s(t)$) are separated, as shown in figures 7(*c*) and 8(*c*) for small- and large-w_0 cases, respectively. The bubble/spike width is scaled as $\eta_{b/s} = k_1[w_{b/s}(t) - Z_c w^0_{0b/0s}]$, in which $w_{0b/0s}$ is the initial bubble/spike width, as listed in table 1. The bubble width of the multi-mode interface in all cases is lower than that of the single-mode counterpart in late stages ($\tau_w \leq 0.5$), which indicates that the mode-competition effect advances the saturation of the bubble evolution in the 2-D multi-mode RM instability. The nonlinear behaviour of the spike of a multi-mode interface is greatly influenced by the initial spectra. In small-w_0 cases, $w_s(t)$ in IP-s and AP-s cases are lower while $w_s(t)$ in k_2AP-s and k_3AP-s cases are higher than those of the single-mode counterpart, which means that the phase of the constituent mode influences the spike behaviour in the 2-D multi-mode RM instability. In large-w_0 cases, $w_s(t)$ in k_3AP-h, k_2AP-h and AP-h cases are close to those of the single-mode counterpart, which indicates that the initial amplitude of the constituent mode influences the spike behaviour. The width growth rates of the bubble $\dot{w}_b(t)$ and the spike $\dot{w}_s(t)$ are calculated, as shown in figures 7(*d*) and 8(*d*) for small- and large-w_0 cases, respectively. The bubble/spike width growth rate is scaled as $\zeta_{b/s} = 2\dot{w}_{b/s}(t)/v_w^{MR}$. It is shown that the bubble width growth rate of a multi-mode interface is generally lower than that of the single-mode counterpart. The spike width growth rate reflects whether the mode-competition effect promotes or suppresses the multi-mode RM instability in early stages.

Since the angle between the incident shock and UP (DP) is zero, no vorticity is deposited at UP (DP). Therefore, UP and DP on the interface remain single-valued until the late nonlinear stage before the transition. As a result, the perturbation width growth of a multi-mode interface can be predicted by superimposing the perturbation growths of initially constituent modes and the generated harmonics at x_{UP} and x_{DP}. In the present coordinate system, the time-varying $w(t)$ growth is superimposed by $w_b(t)$ and $w_s(t)$:

$$w(t) = w_b(t) + w_s(t), \tag{3.12}$$

with

$$w_b(t) = Z_c w_{0b} + \sum_n \int_0^t v_{k_n}^{ln} \cos(k_n x_{\mathrm{DP}})\, \mathrm{d}t, \tag{3.13}$$

$$w_s(t) = Z_c w_{0s} - \sum_n \int_0^t v_{k_n}^{ln} \cos(k_n x_{\mathrm{UP}})\, \mathrm{d}t. \tag{3.14}$$

Case	IP-s	k_3AP-s	k_2AP-s	AP-s	IP-h	k_3AP-h	k_2AP-h	AP-h
$\dot{w}^0_{exp}$	30 ± 2	32 ± 2	39 ± 2	34 ± 2	37 ± 2	36 ± 2	49 ± 2	39 ± 2
$\dot{w}^0_{theo}$	28	29	38	32	34	35	52	41

Table 4. Comparison of the experimental initial perturbation width growth rate ($\dot{w}_{exp}$) of the multi-mode interface with the theoretical counterpart ($\dot{w}_{theo}$) calculated with (3.15).

In this work, (3.12)–(3.14) constitute the 'sum' model which is used to calculate the perturbation width by superimposing the amplitudes of three constituent modes and three generated harmonics. By linear fitting of the perturbation width of a multi-mode interface before 120 μs in all cases, the experimental initial perturbation width growth rate ($\dot{w}^0_{exp}$) can be obtained, as listed in table 4. The theoretical initial perturbation width growth rate of the interface ($\dot{w}^0_{theo}$) can be evaluated by superimposing the amplitude growth rates of three constituent modes and three generated harmonics:

$$\dot{w}^0_{theo} = \sum_{n=1}^{6} v^{ln}_{k_n} [\cos(k_n x_{\mathrm{DP}}) - \cos(k_n x_{\mathrm{UP}})]. \tag{3.15}$$

The values of $\dot{w}^0_{theo}$ in all cases are listed in table 4 and agree well with the experimental results. Then, the predictions of the sum model for $w(t)$, $w_b(t)$ and $w_s(t)$ are shown in figures 7 and 8, and agree well with the experimental counterparts. Meanwhile, the differentiation of the sum model is calculated and compared with the experimental $\dot{w}(t)$, $\dot{w}_b(t)$ and $\dot{w}_s(t)$, and a good agreement is also achieved between them. Note that there are several break points, for example in k_3AP-h and AP-h cases, when the sum model is used to predict the growth rates, which is ascribed to the enforced post-saturation treatment adopted when v^{en}_k is calculated. After the incident shock wave impacts the interface, the transverse waves between the transmitted shock and reflected shock interact with the interface, especially when the initial interface perturbation is prominent. Therefore, the non-uniform flow influences the linear interface growth (Guo *et al.* 2020), resulting in the perturbation width growth varying around the sum model prediction at an early regime.

To further validate the sum model, the experimental results with M (= 1.3) and A^+ (= 0.67) similar to our experiments extracted from figure 4(*a*) in Sadot *et al.* (1998) are adopted as shown in figure 9(*a*). The initial interface is a two-bubble interface, which is dominated by the first five order modes: $a^0_{k_1} = 1.49 \times 10^{-3}$, $a^0_{k_2} = 1.06 \times 10^{-3}$, $a^0_{k_3} = 0.40 \times 10^{-3}$, $a^0_{k_4} = 0.21 \times 10^{-3}$, $a^0_{k_5} = 0.10 \times 10^{-3}$ m; $k_1 = 180\,\mathrm{m}^{-1}$, $k_i = ik_1$ with i = 2–5; $\phi_1 = \pi$, $\phi_2 = \phi_3 = \phi_4 = \phi_5 = 0$; $R_{k_1} = 0.92$, $R_{k_2} = 0.89$, $R_{k_3} = 0.93$, $R_{k_4} = 0.95$ and $R_{k_5} = 0.97$; $\beta = 0.49$. The amplitudes of the five constituent modes and five generated harmonics are calculated by the present model, and then superimposed according to the sum model. One can see that the predictions of the sum model agree well with both the large bubble width and the small bubble width. Besides, the experimental results with M (= 1.2) and A^+ (= 0.6) similar to our experiments extracted from figure 9 in Luo *et al.* (2019) are shown in figure 9(*b*). For the CS-1 case (ICS-2 case), the initial interface is a spike-dominated (bubble-dominated) chevron-shaped interface, which is dominated by the first five order modes: $a^0_{k_1} = 1.08 \times 10^{-3}$, $a^0_{k_2} = 0.81 \times 10^{-3}$, $a^0_{k_3} = 0.48 \times 10^{-3}$, $a^0_{k_4} = 0.20 \times 10^{-3}$, $a^0_{k_5} = 0.04 \times 10^{-3}$ m; $k_1 = 52\,\mathrm{m}^{-1}$, $k_i = ik_1$ with i = 2–5; for the CS-1 case, $\phi_1 = \phi_3 = \phi_5 = 0$, $\phi_2 = \phi_4 = \pi$; for the ICS-2 case, $\phi_1 =$

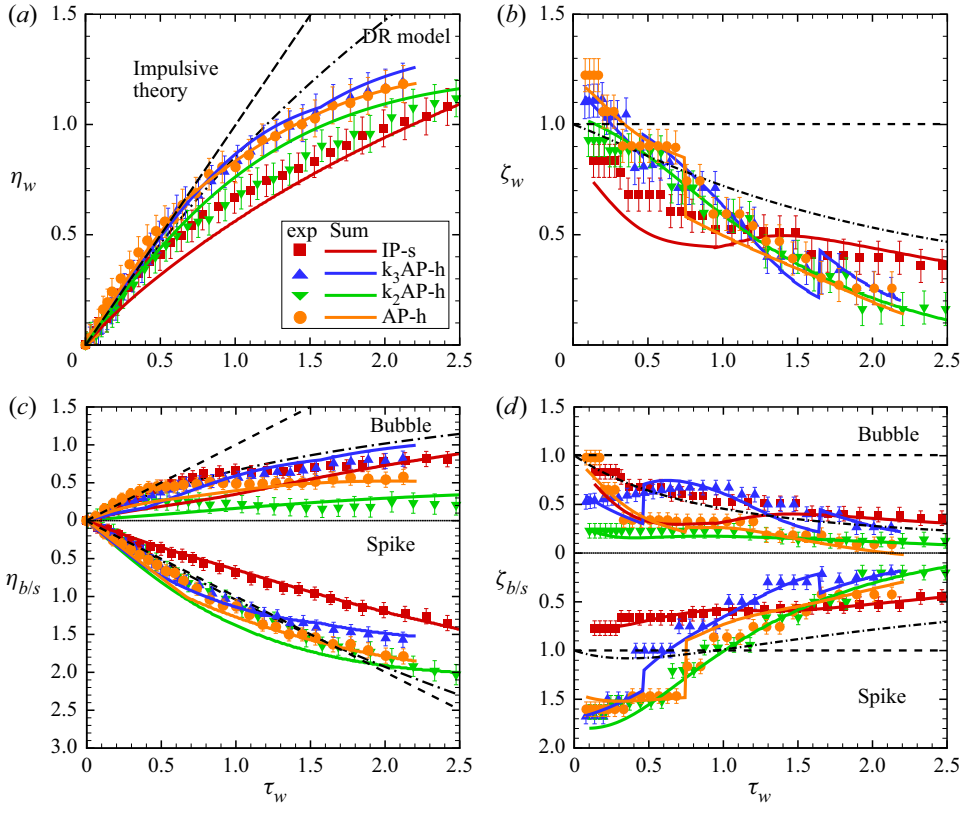

Figure 8. Comparison of the perturbation width (*a*), growth rate of the perturbation width (*b*), widths of bubble and spike (*c*) and width growth rates of bubble and spike (*d*) in large-w_0 cases.

$\phi_3 = \phi_5 = \pi$, $\phi_2 = \phi_4 = 0$. For these two cases, $R_{k_1} = 0.98$, $R_{k_2} = 0.97$, $R_{k_3} = 0.98$, $R_{k_4} = 0.99$ and $R_{k_5} = 1.0$; $\beta = 0.67$. The amplitudes of the five constituent modes and five generated harmonics are calculated and the sum model well predicts the experimental results. Moreover, the numerical results with M (= 5) and A^+ (= 0.95) much larger than in our experiments extracted from figure 4 in Pandian *et al.* (2017) are shown in figure 9(*c*). The initial interface consists of two modes: $a^0_{k_1} = a^0_{k_2} = 1.1 \times 10^{-3}$ m; $k_1 = 1.885 \times 10^3\ \mathrm{m}^{-1}$, $k_2 = 2k_1$; $\phi_1 = \pi$, $\phi_2 = 0$; $R_{k_1} = 0.59$, $R_{k_2} = 0.42$; $\beta = 0.26$. The amplitudes of the two constituent modes and two generated harmonics are calculated and the sum model also well predicts the numerical results. All these agreements achieved demonstrate the generality of the sum model.

4. Conclusions

In this work, a 2-D complex multi-mode interface constituted of various modes is first formed by the soap-film technique, and then elaborate shock-tube experiments on the developments of eight kinds of air–SF_6 multi-mode interface are performed. Based on these well-controlled experiments and several theories in the literature, a general nonlinear theory is established for predicting multi-mode evolution and mixing, and

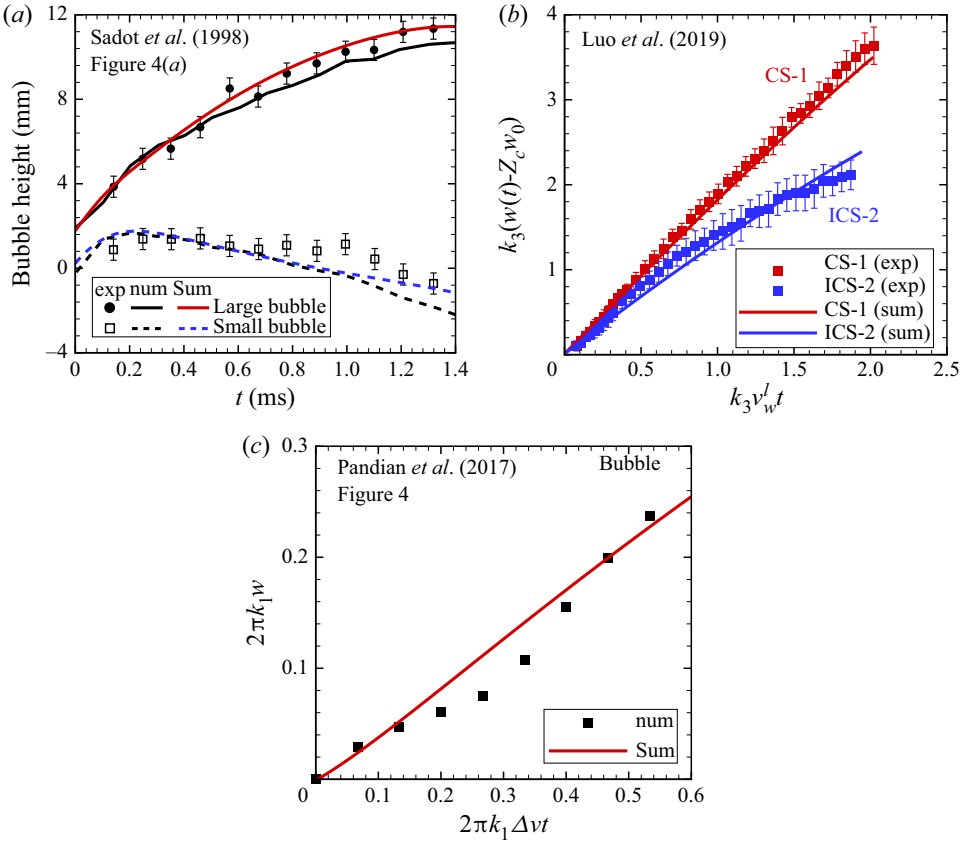

Figure 9. The perturbation width of the multi-mode interface obtained from (*a*) the experiments and simulations in Sadot *et al.* (1998), (*b*) the experiments in Luo *et al.* (2019) and (*c*) the simulations in Pandian *et al.* (2017).

finally a quantitative relation between the initial conditions and the perturbation growth is constructed.

From the schlieren images of the shocked multi-mode interface, it is found that the phases of the constituent modes greatly affect the initial interface shape and the later interface evolution. It is also found that the transition from linear to nonlinear may occur earlier when the initial interface amplitude is larger. By considering different wavenumbers, initial amplitudes and phases of constituent modes, the dependence of the perturbation growth on initial spectra is highlighted.

The captured interface morphology is distinct such that the interface contours in all cases can be easily extracted by an image processing program. Subsequently, spectrum analysis is performed on the interface contour before the interface becomes multi-valued, and amplitudes of constituent modes are then acquired. It is first proved that the mode-competition effect influences the amplitude growth of each mode from the very beginning (quasi-linear stage), especially when the initial amplitudes of constituent modes are large. It is interesting that the mode competition starts to play a role at this quasi-linear stage although the growing of harmonics is so small as to be negligible. Therefore our findings differ from previous views. The mode-competition effect is closely associated with the initial spectra.

A nonlinear theory is constructed by considering both the mode-competition effect and the high-order harmonics effect to predict the amplitude growth of the modes. The new theory has been validated by our experiments and data in the literature with the consideration of diverse constituent modes, and a wide range of Mach number and Atwood number. Further, the nonlinear theory is extended based on the superposition principle to predict the growths of the total perturbation width and spike/bubble width, and there is a satisfactory agreement between the predictions and the experimental results. It can be concluded that the evolution of the shocked multi-mode interface has an evident memory of the initial conditions from quasi-linear to late nonlinear stages.

The RM instability at the fully turbulent state has been a focus of attention recently. We will combine the soap-film technique with a time-resolved particle image velocimetry system to investigate the multi-mode RM instability induced by one shock or two shocks in the near future. Besides, we look forward to examining the models established in this work with experiments involving very high Atwood numbers.

Acknowledgements. The authors appreciate the valuable suggestions of the reviewers.

Funding. This work was supported by the Natural Science Foundation of China (nos. 91952205, 12022201, 11772329, 11625211 and 11621202) and Tamkeen under NYU Abu Dhabi Research Institute grant CG002.

Declaration of interests. The authors report no conflict of interest.

Author ORCIDs.
Yu Liang https://orcid.org/0000-0002-3254-7073;
Zhigang Zhai https://orcid.org/0000-0002-0094-5210;
Juchun Ding https://orcid.org/0000-0001-6578-1694;
Ting Si https://orcid.org/0000-0001-9071-8646;
Xisheng Luo https://orcid.org/0000-0002-4303-8290.

References

Abarzhi, S.I. 2008 Coherent structures and pattern formation in Rayleigh–Taylor turbulent mixing. *Phys. Scr.* **78** (1), 015401.

Abarzhi, S.I. 2010 Review of theoretical modelling approaches of Rayleigh–Taylor instabilities and turbulent mixing. *Phil. Trans. R. Soc.* A **368** (1916), 1809–1828.

Alon, U., Hecht, J., Mukamel, D. & Shvarts, D. 1994 Scale invariant mixing rates of hydrodynamically unstable interface. *Phys. Rev. Lett.* **72**, 2867–2870.

Alon, U., Hecht, J., Ofer, D. & Shvarts, D. 1995 Power laws and similarity of Rayleigh–Taylor and Richtmyer-Meshkov mixing fronts. *Phys. Rev. Lett.* **74**, 534–537.

Balasubramanian, S., Orlicz, G.C. & Prestridge, K.P. 2013 Experimental study of initial condition dependence on turbulent mixing in shock-accelerated Richtmyer-Meshkov fluid layers. *J. Turbul.* **14** (3), 170–196.

Brouillette, M. 2002 The Richtmyer-Meshkov instability. *Annu. Rev. Fluid Mech.* **34**, 445–468.

Chandrasekhar, S. 2013 *Hydrodynamic and Hydromagnetic Stability*. Courier Corporation.

Cohen, R.D. 1991 Shattering of a liquid drop due to impact. *Proc. R. Soc. Lond.* A **435**, 483–503.

Collins, B.D. & Jacobs, J.W. 2002 PLIF flow visualization and measurements of the Richtmyer-Meshkov instability of an air/SF_6 interface. *J. Fluid Mech.* **464**, 113–136.

Dell, Z., Stellingwerf, R.F. & Abarzhi, S.I. 2015 Effect of initial perturbation amplitude on Richtmyer-Meshkov flows induced by strong shocks. *Phys. Plasmas* **22** (9), 092711.

Dell, Z.R., Pandian, A., Bhowmick, A.K., Swisher, N.C., Stanic, M., Stellingwerf, R.F. & Abarzhi, S.I. 2017 Maximum initial growth-rate of strong-shock-driven Richtmyer-Meshkov instability. *Phys. Plasmas* **24** (9), 090702.

Di Stefano, C.A., Malamud, G., Kuranz, C.C., Klein, S.R. & Drake, R.P. 2015*a* Measurement of Richtmyer-Meshkov mode coupling under steady shock conditions and at high energy density. *High Energy Density Phys.* **17**, 263–269.

DI STEFANO, C.A., MALAMUD, G., KURANZ, C.C., KLEIN, S.R., STOECKL, C. & DRAKE, R.P. 2015*b* Richtmyer-Meshkov evolution under steady shock conditions in the high-energy-density regime. *Appl. Phys. Lett.* **106** (11), 114103.

DIMONTE, G., FRERKING, C.E., SCHNEIDER, M. & REMINGTON, B. 1996 Richtmyer-Meshkov instability with strong radiatively driven shocks. *Phys. Plasmas* **3** (2), 614–630.

DIMONTE, G. & RAMAPRABHU, P. 2010 Simulations and model of the nonlinear Richtmyer-Meshkov instability. *Phys. Fluids* **22**, 014104.

DIMONTE, G. & SCHNEIDER, M. 2000 Density ratio dependence of Rayleigh–Taylor mixing for sustained and impulsive acceleration histories. *Phys. Fluids* **12**, 304–321.

DING, J.C., SI, T., CHEN, M.J., ZHAI, Z.G., LU, X.Y. & LUO, X.S. 2017 On the interaction of a planar shock with a three-dimensional light gas cylinder. *J. Fluid Mech.* **828**, 289–317.

DRAZIN, P.G. & REID, W.H. 2004 *Hydrodynamic Stability*. Cambridge University Press.

ELBAZ, Y. & SHVARTS, D. 2018 Modal model mean field self-similar solutions to the asymptotic evolution of Rayleigh–Taylor and Richtmyer-Meshkov instabilities and its dependence on the initial conditions. *Phys. Plasmas* **25** (6), 062126.

GONCHAROV, V.N. 1999 Theory of the ablative Richtmyer-Meshkov instability. *Phys. Rev. Lett.* **82** (10), 2091.

GROOM, M. & THORNBER, B. 2020 The influence of initial perturbation power spectra on the growth of a turbulent mixing layer induced by Richtmyer-Meshkov instability. *Physica* D **407**, 132463.

GUO, X., ZHAI, Z., DING, J., SI, T. & LUO, X. 2020 Effects of transverse shock waves on early evolution of multi-mode chevron interface. *Phys. Fluids* **32** (10), 106101.

HAAN, S.W. 1989 Onset of nonlinear saturation for Rayleigh–Taylor growth in the presence of a full spectrum of modes. *Phys. Rev.* A **39** (11), 5812.

HAAN, S.W. 1991 Weakly nonlinear hydrodynamic instabilities in inertial fusion. *Phys. Fluids* B **3**, 2349–2355.

HECHT, J., ALON, U. & SHVARTS, D. 1994 Potential flow models of Rayleigh–Taylor and Richtmyer-Meshkov bubble fronts. *Phys. Fluids* **6**, 4019–4030.

HOSSEINI, S.H.R. & TAKAYAMA, K. 2005 Experimental study of Richtmyer-Meshkov instability induced by cylindrical shock waves. *Phys. Fluids* **17**, 084101.

HURRICANE, O.A., BURKE, E., MAPLES, S. & VISWANATHAN, M. 2000 Saturation of Richtmyer's impulsive model. *Phys. Fluids* **12** (8), 2148–2151.

JACOBS, J.W. & KRIVETS, V.V. 2005 Experiments on the late-time development of single-mode Richtmyer-Meshkov instability. *Phys. Fluids* **17**, 034105.

JACOBS, J.W. & SHEELEY, J.M. 1996 Experimental study of incompressible Richtmyer-Meshkov instability. *Phys. Fluids* **8**, 405–415.

KURANZ, C.C., *et al.* 2018 How high energy fluxes may affect Rayleigh–Taylor instability growth in young supernova remnants. *Nat. Commun.* **9**, 1564.

LAYZER, D. 1955 On the instability of superposed fluids in a gravitational field. *Astrophys. J.* **122**, 1–12.

LEI, F., DING, J., SI, T., ZHAI, Z. & LUO, X. 2017 Experimental study on a sinusoidal air/SF_6 interface accelerated by a cylindrically converging shock. *J. Fluid Mech.* **826**, 819–829.

LIANG, Y., LIU, L., ZHAI, Z., SI, T. & LUO, X. 2021 Universal perturbation growth of Richtmyer-Meshkov instability for minimum-surface featured interface induced by weak shock waves. *Phys. Fluids* **33** (3), 032110.

LIANG, Y., ZHAI, Z., DING, J. & LUO, X. 2019 Richtmyer-Meshkov instability on a quasi-single-mode interface. *J. Fluid Mech.* **872**, 729–751.

LINDL, J., LANDEN, O., EDWARDS, J., MOSES, E. & TEAM, N. 2014 Review of the national ignition campaign 2009–2012. *Phys. Plasmas* **21**, 020501.

LIU, H. & XIAO, Z. 2016 Scale-to-scale energy transfer in mixing flow induced by the Richtmyer-Meshkov instability. *Phys. Rev.* E **93** (5), 053112.

LIU, L., LIANG, Y., DING, J., LIU, N. & LUO, X. 2018 An elaborate experiment on the single-mode Richtmyer-Meshkov instability. *J. Fluid Mech.* **853**, R2.

LUO, X., LIANG, Y., SI, T. & ZHAI, Z. 2019 Effects of non-periodic portions of interface on Richtmyer-Meshkov instability. *J. Fluid Mech.* **861**, 309–327.

LUO, X., LIU, L., LIANG, Y., DING, J. & WEN, C.Y. 2020 Richtmyer-Meshkov instability on a dual-mode interface. *J. Fluid Mech.* **905**, A5.

LUO, X., WANG, X. & SI, T. 2013 The Richtmyer-Meshkov instability of a three-dimensional air/SF_6 interface with a minimum-surface feature. *J. Fluid Mech.* **722**, R2.

LUO, X., WANG, M., SI, T. & ZHAI, Z. 2015 On the interaction of a planar shock with an SF_6 polygon. *J. Fluid Mech.* **773** (2), 366–394.

MANSOOR, M.M., DALTON, S.M., MARTINEZ, A.A., DESJARDINS, T., CHARONKO, J.J. & PRESTRIDGE, K.P. 2020 The effect of initial conditions on mixing transition of the Richtmyer-Meshkov instability. *J. Fluid Mech.* **904**, A3.

MARIANI, C., VANDENBOOMGAERDE, M., JOURDAN, G., SOUFFLAND, D. & HOUAS, L. 2008 Investigation of the Richtmyer-Meshkov instability with stereolithographed interfaces. *Phys. Rev. Lett.* **100**, 254503.

MESHKOV, E.E. 1969 Instability of the interface of two gases accelerated by a shock wave. *Fluid Dyn.* **4**, 101–104.

MEYER, K.A. & BLEWETT, P.J. 1972 Numerical investigation of the stability of a shock-accelerated interface between two fluids. *Phys. Fluids* **15**, 753–759.

MIKAELIAN, K.O. 1998 Analytic approach to nonlinear Rayleigh–Taylor and Richtmyer-Meshkov instabilities. *Phys. Rev. Lett.* **80**, 508–511.

MIKAELIAN, K.O. 2003 Explicit expressions for the evolution of single-mode Rayleigh–Taylor and Richtmyer-Meshkov instabilities at arbitrary Atwood numbers. *Phys. Rev.* E **67**, 026319.

MIKAELIAN, K.O. 2005 Richtmyer-Meshkov instability of arbitrary shapes. *Phys. Fluids* **17**, 034101.

MILES, A.R., EDWARDS, M.J., BLUE, B., HANSEN, J.F., ROBEY, H.F., DRAKE, R.P., KURANZ, C. & LEIBRANDT, D.R. 2004 The effects of a short-wavelength mode on the evolution of a long-wavelength perturbatoin driven by a strong blast wave. *Phys. Plasmas* **11**, 5507–5519.

MOHAGHAR, M., CARTER, J., MUSCI, B., REILLY, D., MCFARLAND, J.A. & RANJAN, D. 2017 Evaluation of turbulent mixing transition in a shock-driven variable-density flow. *J. Fluid Mech.* **831**, 779–825.

MOHAGHAR, M., CARTER, J., PATHIKONDA, G. & RANJAN, D. 2019 The transition to turbulence in shock-driven mixing: effects of Mach number and initial conditions. *J. Fluid Mech.* **871**, 595–635.

MÜGLER, C. & GAUTHIER, S. 1998 Numerical simulations of single-mode Richtmyer-Meshkov experiments. *Phys. Rev.* E **58** (4), 4548.

NIEDERHAUS, C.E. & JACOBS, J.W. 2003 Experimental study of the Richtmyer-Meshkov instability of incompressible fluids. *J. Fluid Mech.* **485**, 243–277.

NISHIHARA, K., WOUCHUK, J.G., MATSUOKA, C., ISHIZAKI, R. & ZHAKHOVSKY, V.V. 2010 Richtmyer-Meshkov instability: theory of linear and nonlinear evolution. *Phil. Trans. R. Soc.* A **368**, 1769–1807.

OFER, D., ALON, U., SHVARTS, D., MCCRORY, R.L. & VERDON, C.P. 1996 Modal model for the nonlinear multimode Rayleigh–Taylor instability. *Phys. Plasmas* **3** (8), 3073–3090.

ORON, D., ARAZI, L., KARTOON, D., RIKANATI, A., ALON, U. & SHVARTS, D. 2001 Dimensionality dependence of the Rayleigh–Taylor and Richtmyer-Meshkov instability late-time scaling laws. *Phys. Plasmas* **8**, 2883–2889.

PANDIAN, A., STELLINGWERF, R.F. & ABARZHI, S.I. 2017 Effect of a relative phase of waves constituting the initial perturbation and the wave interference on the dynamics of strong-shock-driven Richtmyer-Meshkov flows. *Phys. Rev. Fluids* **2** (7), 073903.

RANJAN, D., ANDERSON, M., OAKLEY, J. & BONAZZA, R. 2005 Experimental investigation of a strongly shocked gas bubble. *Phys. Rev. Lett.* **94**, 184507.

RAYLEIGH, L. 1883 Investigation of the character of the equilibrium of an incompressible heavy fluid of variable density. *Proc. Lond. Math. Soc.* **14**, 170–177.

REMINGTON, B.A., WEBER, S.V., MARINAK, M.M., HAAN, S.W., KILKENNY, J.D., WALLACE, R.J. & DIMONTE, G 1995 Single-mode and multimode Rayleigh–Taylor experiments on nova. *Phys. Plasmas* **2** (1), 241–255.

RICHTMYER, R.D. 1960 Taylor instability in shock acceleration of compressible fluids. *Commun. Pure Appl. Maths* **13**, 297–319.

RIKANATI, A., ALON, U. & SHVARTS, D. 1998 Vortex model for the nonlinear evolution of the multimode Richtmyer-Meshkov instability at low Atwood numbers. *Phys. Rev.* E **58**, 7410–7418.

RIKANATI, A., ORON, D., SADOT, O. & SHVARTS, D. 2003 High initial amplitude and high Mach number effects on the evolution of the single-mode Richtmyer-Meshkov instability. *Phys. Rev.* E **67**, 026307.

SADOT, O., EREZ, L., ALON, U., ORON, D., LEVIN, L.A., EREZ, G., BEN-DOR, G. & SHVARTS, D. 1998 Study of nonlinear evolution of single-mode and two-bubble interaction under Richtmyer-Meshkov instability. *Phys. Rev. Lett.* **80**, 1654–1657.

SEWELL, E.G., FERGUSON, K.J., KRIVETS, V.V. & JACOBS, J.W. 2021 Time-resolved particle image velocimetry measurements of the turbulent Richtmyer–Meshkov instability. *J. Fluid Mech.* **917**, A41.

SI, T., LONG, T., ZHAI, Z. & LUO, X. 2015 Experimental investigation of cylindrical converging shock waves interacting with a polygonal heavy gas cylinder. *J. Fluid Mech.* **784**, 225–251.

TAYLOR, G. 1950 The instability of liquid surfaces when accelerated in a direction perpendicular to their planes. I. *Proc. R. Soc. Lond.* A **201** (1065), 192–196.

THORNBER, B. 2016 Impact of domain size and statistical errors in simulations of homogeneous decaying turbulence and the Richtmyer-Meshkov instability. *Phys. Fluids* **28** (4), 045106.

THORNBER, B., DRIKAKIS, D., YOUNGS, D.L. & WILLIAMS, R.J.R. 2010 The influence of initial condition on turbulent mixing due to Richtmyer-Meshkov instability. *J. Fluid Mech.* **654**, 99–139.

VANDENBOOMGAERDE, M., GAUTHIER, S. & MÜGLER, C. 2002 Nonlinear regime of a multimode Richtmyer-Meshkov instability: a simplified perturbation theory. *Phys. Fluids* **14** (3), 1111–1122.

VANDENBOOMGAERDE, M., SOUFFLAND, D., MARIANI, C., BIAMINO, L., JOURDAN, G. & HOUAS, L. 2014 An experimental and numerical investigation of the dependency on the initial conditions of the Richtmyer-Meshkov instability. *Phys. Fluids* **26**, 024109.

VELIKOVICH, A., HERRMANN, M. & ABARZHI, S. 2014 Perturbation theory and numerical modelling of weakly and moderately nonlinear dynamics of the incompressible Richtmyer-Meshkov instability. *J. Fluid Mech.* **751**, 432–479.

VELIKOVICH, A.L. & DIMONTE, G. 1996 Nonlinear perturbation theory of the incompressible Richtmyer-Meshkov instability. *Phys. Rev. Lett.* **76** (17), 3112.

ZHAI, Z., DONG, P., SI, T. & LUO, X. 2016 The Richtmyer-Meshkov instability of a V shaped air/helium interface subjected to a weak shock. *Phys. Fluids* **28** (8), 082104.

ZHAI, Z., WANG, M., SI, T. & LUO, X. 2014 On the interaction of a planar shock with a light SF_6 polygonal interface. *J. Fluid Mech.* **757** (2), 800–816.

ZHAI, Z., ZOU, L., WU, Q. & LUO, X. 2018 Review of experimental Richtmyer-Meshkov instability in shock tube: from simple to complex. *Proc. Inst. Mech. Engrs* C **232**, 2830–2849.

ZHANG, Q. & SOHN, S.I. 1997 Nonlinear theory of unstable fluid mixing driven by shock wave. *Phys. Fluids* **9**, 1106–1124.

ZHOU, Y. 2007 Unification and extension of the similarity scaling criteria and mixing transition for studying astrophysics using high energy density laboratory experiments or numerical simulations. *Phys. Plasmas* **14** (8), 082701.

ZHOU, Y. 2017*a* Rayleigh–Taylor and Richtmyer-Meshkov instability induced flow, turbulence, and mixing. I. *Phys. Rep.* **720–722**, 1–136.

ZHOU, Y. 2017*b* Rayleigh–Taylor and Richtmyer-Meshkov instability induced flow, turbulence, and mixing. II. *Phys. Rep.* **723–725**, 1–160.

ZHOU, Y., CLARK, T.T., CLARK, D.S., GLENDINNING, S.S., SKINNER, A.A., HUNTINGTON, C., HURRICANE, O.A., DIMITS, A.M. & REMINGTON, B.A. 2019 Turbulent mixing and transition criteria of flows induced by hydrodynamic instabilities. *Phys. Plasmas* **26** (8), 080901.

ZHOU, Y., ROBEY, H.F. & BUCKINGHAM, A.C. 2003 Onset of turbulence in accelerated high-Reynolds-number flow. *Phys. Rev.* E **67** (5), 056305.